

Ultrathin and Small-Size Graphene Oxide as an Electron Mediator for Perovskite-Based Z-Scheme System to Significantly Enhance Photocatalytic CO₂ Reduction

Yan-Fei Mu, Wen Zhang, Guang-Xing Dong, Ke Su, Min Zhang,* and Tong-Bu Lu

The judicious design of efficient electron mediators to accelerate the interfacial charge transfer in a Z-scheme system is one of the viable strategies to improve the performance of photocatalysts for artificial photosynthesis. Herein, ultrathin and small-size graphene oxide (USGO) nanosheets are constructed and employed as the electron mediator to elaborately exploit an efficient CsPbBr₃-based all-solid-state Z-scheme system in combination with α -Fe₂O₃ for visible-light-driven CO₂ reduction with water as the electron source. CsPbBr₃ and α -Fe₂O₃ can be closely anchored on USGO nanosheets, owing to the existence of interfacial strong chemical bonding behaviors, which can significantly accelerate the photogenerated carrier transfer between CsPbBr₃ and α -Fe₂O₃. The resultant improved charge separation efficiency endows the Z-scheme system exhibiting a record-high electron consumption rate of 147.6 $\mu\text{mol g}^{-1} \text{h}^{-1}$ for photocatalytic CO₂-to-CO conversion concomitant with stoichiometric O₂ from water oxidation, which is over 19 and 12 times higher than that of pristine CsPbBr₃ nanocrystals and the mixture of CsPbBr₃ and α -Fe₂O₃, respectively. This work provides a novel and effective strategy for improving the catalytic activity of halide-perovskite-based photocatalysts, promoting their practical applications in the field of artificial photosynthesis.

1. Introduction

Inspired by natural photosynthesis, the use of sunlight-driven CO₂ reduction over photocatalysts with water as electron source to produce fuels or high-value added chemical feedstocks is one of promising approaches to surmount the energy and

environmental crises.^[1–10] The economic efficiency of this artificial photosynthesis technology could be attained by resorting to the development of cost-effective photocatalytic systems. In this regard, halide perovskite nanocrystals (NCs), a kind of fascinating light-harvesting materials possessing low-cost fabrication techniques and excellent optoelectronic properties such as large extinction coefficients and long photogenerated carrier lifetime,^[11–13] have been demonstrated to be able to achieve visible-light-driven CO₂ reduction concomitant with desirable water oxidation recently,^[14–16] exhibiting great potential in the field of practical artificial photosynthesis. However, this kind of semiconductor NCs in its pristine form generally displays very low activity for photocatalytic CO₂ reduction, due to the insufficient charge separation and the lack of intrinsic catalytic sites.

Recently, continuous efforts have been devoted to enhance the activity of perovskite nanocrystals for photocatalytic CO₂ reduction, such as loading perovskite NCs on graphene oxide^[17] or g-C₃N₄^[18] to improve the photogenerated carrier separation, designing appropriate heterojunction with other materials involving abundant active sites,^[14,15] or directly doping metal active sites on the surface of perovskite NCs.^[19] However, these strategies only concern about the CO₂ reduction half-reaction, and the H₂O oxidation half-reaction has attracted little attention, the latter of which also plays a pivotal role in controlling the overall performance. In this context, constructing appropriate Z-scheme system^[20–22] with halide perovskite NCs and another oxygen evolution photocatalysts could be one of feasible strategies to improve the photogenerated carrier separation and enhance the water oxidation ability, which has not gained sufficient attention for perovskite NCs.^[23]

The effectiveness of Z-scheme systems relies on the judicious design of efficient electron mediators to achieve fast interfacial charge transfer.^[24–29] Herein, we have elaborately designed ultrathin and small-size graphene oxide (USGO) nanosheet and employed it as electron mediator to exploit an efficient CsPbBr₃-based all-solid-state Z-scheme system in combination with hematite (coded as CsPbBr₃/USGO/ α -Fe₂O₃) for visible-light-driven CO₂ reduction. Our strategy is based on the following important considerations: 1) From an economic

Y.-F. Mu, Dr. W. Zhang, G.-X. Dong, K. Su, Prof. M. Zhang, Prof. T.-B. Lu
MOE International Joint Laboratory of Materials Microstructure
Tianjin University of Technology
Tianjin 300384, China
E-mail: zm2016@email.tjut.edu.cn

Y.-F. Mu, Dr. W. Zhang, G.-X. Dong, K. Su, Prof. M. Zhang, Prof. T.-B. Lu
Institute for New Energy Materials and Low Carbon Technologies
School of Materials Science and Engineering
Tianjin University of Technology
Tianjin 300384, China

Prof. M. Zhang
Tianjin Key Laboratory of Organic Solar Cells and Photochemical
Conversion, School of Chemistry and Chemical Engineering
Tianjin University of Technology
Tianjin 300384, China

 The ORCID identification number(s) for the author(s) of this article can be found under <https://doi.org/10.1002/sml.202002140>.

DOI: 10.1002/sml.202002140

viewpoint, α -Fe₂O₃ is an ideal material for photocatalytic water oxidation, owing to its inexpensive fabrication techniques, high chemical stability, and suitable band structure for visible-light response and triggering water oxidation reaction.^[30–34] 2) The 2D graphene material is a promising electron transfer mediator owing to its excellent electron transport mobility,^[35,36] which can accelerate the charge transfer between CsPbBr₃ and α -Fe₂O₃, thus improving the photogenerated carrier separation efficiency. 3) There are abundant functional groups such as carboxyl and hydroxyl in the surface of USGO,^[37] which can form strong chemical bonds with CsPbBr₃,^[38–40] facilitating CsPbBr₃ loading and photogenerated electron transfer from CsPbBr₃ to graphene oxide. As expected, this CsPbBr₃/USGO/ α -Fe₂O₃ Z-scheme photocatalyst system achieves efficient charge transfer between CsPbBr₃ and α -Fe₂O₃, exhibiting significantly improved photocatalytic activity for CO₂ conversion in a reaction system with water as electron source, which is over 19 times higher than that of pristine CsPbBr₃ nanocrystals.

2. Results and Discussion

The USGO nanosheets were synthesized with modified methods of predecessors^[41,42] by controlling the amount of oxidants and oxidation time, and the details are described in the Supporting Information. The mean size of as-prepared USGO nanosheets can be obtained based on the analysis of atomic force microscopy (AFM) image of USGO (Figure 1a), being \approx 200–400 nm. Further analysis of the corresponding height cross-sectional profile of USGO (Figure 1b) displays that the mean height of USGO sheets is \approx 0.75 nm, indicating that a fully exfoliated ultrathin graphene oxide nanosheet was successfully prepared.^[43] The corresponding IR spectrum of as-prepared USGO (Figure S1, Supporting Information) shows the main characteristic absorption peaks of graphene oxide, featuring abundant oxygen-containing functional groups. X-ray diffraction (XRD) pattern of USGO (Figure S2, Supporting

Information) further demonstrates the formation of graphene oxide with small size, exhibiting a weak and broad diffraction peak at $2\theta = 12.1^\circ$ without the typical diffraction peak of native graphite.^[41]

Zeta potential (ζ) of as-prepared USGO dispersed in hexane was further measured, being -67 mV, which is reversed with those of α -Fe₂O₃ (30 mV) and CsPbBr₃ (27 mV) in the same condition (Figure 1c). The opposite charge nature of USGO surface in comparison with those of α -Fe₂O₃ and CsPbBr₃ should facilitate the spontaneous assembly of α -Fe₂O₃ and CsPbBr₃ on the surface of USGO. The prepared processes of CsPbBr₃/USGO/ α -Fe₂O₃ Z-scheme are illustrated in Figure 1d, and the detailed information regarding the preparation processes is described in the Supporting Information. In brief, the Fe₂O₃ semiconductor was firstly anchored on the as-prepared USGO nanosheets through a hydrothermal process to oxidize Fe₃O₄ nanoparticle precursor.^[44] The XRD pattern (Figure 1e) of as-prepared Fe₂O₃ anchoring on the USGO displays typical diffraction peaks for α -Fe₂O₃ phase (JCPDS: 00-033-0664).^[45] The resulting USGO/ α -Fe₂O₃ composite also exhibits negative charge property with a ζ value of -32 mV (Figure 1c), which was then mixed with as-prepared uniform cubic CsPbBr₃ (Figure S3, Supporting Information) in hexane solvent to easily generate the final CsPbBr₃/USGO/ α -Fe₂O₃ composite through electrostatic self-assembly (Figure S4, Supporting Information). XRD pattern of CsPbBr₃/USGO/ α -Fe₂O₃ (Figure 1e) demonstrates the successful loading of CsPbBr₃ on USGO/ α -Fe₂O₃, which contains the typical diffraction peaks of CsPbBr₃ with cubic phase (JCPDS: 00-054-0572).

The morphology and composition of CsPbBr₃/USGO/ α -Fe₂O₃ were firstly inspected by transmission electron microscopy (TEM) measurement. As presented in Figure 2a, cubic CsPbBr₃ and rod-like α -Fe₂O₃ can be perceptibly observed on the USGO nanosheet. It can be seen that α -Fe₂O₃ nanorods are clustered on the surface USGO nanosheet, while CsPbBr₃ nanocubes are homogeneous elsewhere on the surface of USGO nanosheet, which can be further illustrated from the element

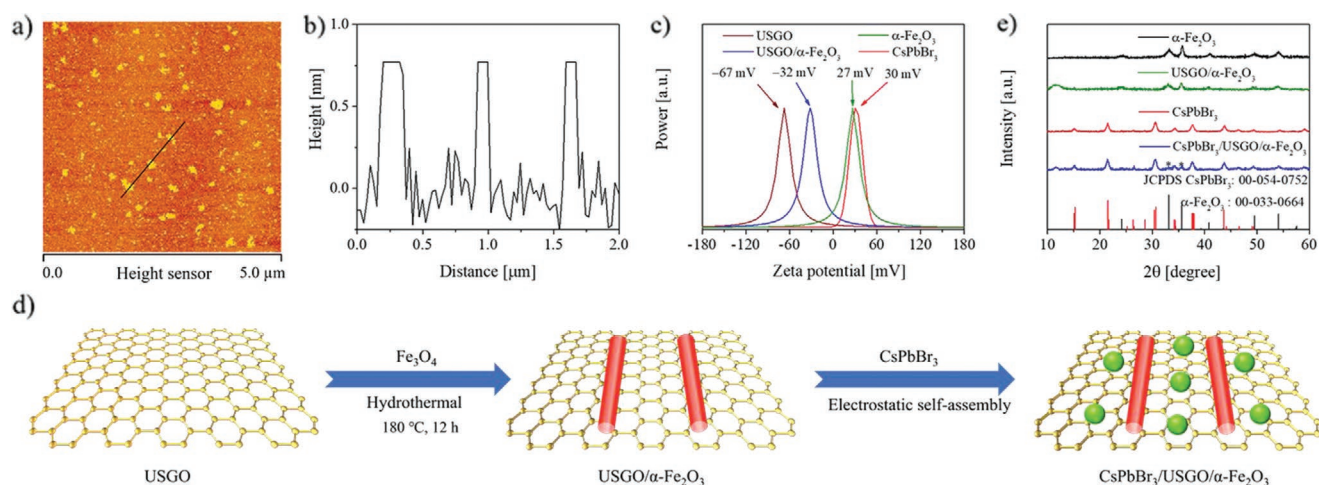


Figure 1. a) Typical tapping mode AFM image and b) the corresponding height cross-sectional profile of USGO deposited on the mica substrate. The mean height of most USGO sheets is \approx 0.75 nm. c) Zeta potentials of as-prepared CsPbBr₃, α -Fe₂O₃, USGO, and USGO/ α -Fe₂O₃ in hexane. d) Schematic illustrations for the synthesis processes of CsPbBr₃/USGO/ α -Fe₂O₃. e) XRD patterns of as-prepared α -Fe₂O₃, USGO/ α -Fe₂O₃, CsPbBr₃/USGO/ α -Fe₂O₃, and CsPbBr₃ powders.

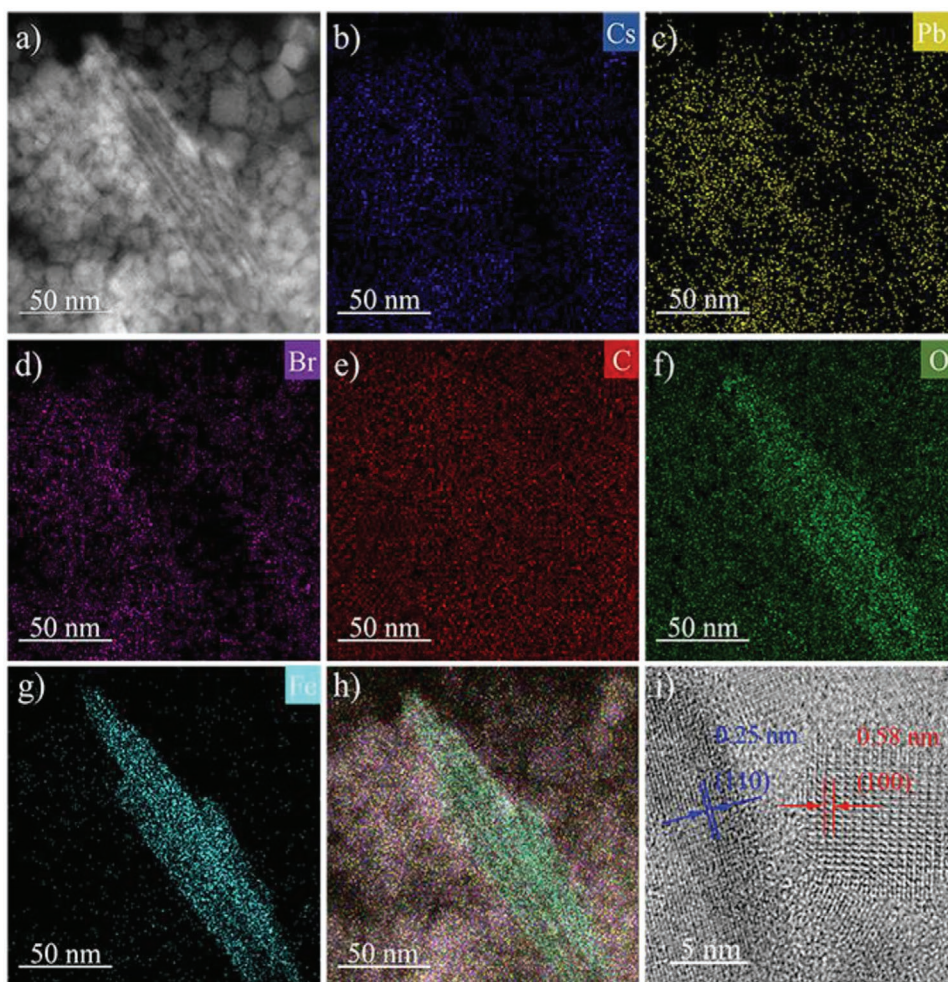


Figure 2. a) TEM image, b–h) elemental mappings, and i) HRTEM image with lattice spacing of as-prepared CsPbBr₃/USGO/ α -Fe₂O₃.

mappings of CsPbBr₃/USGO/ α -Fe₂O₃ composite (Figure 2b–h). Further high-resolution TEM (HRTEM) measurement (Figure 2i) confirmed the presence of α -Fe₂O₃ and CsPbBr₃ on the surface of USGO nanosheet, exhibiting clear lattice fringes of 0.25 nm for (110) plane of α -Fe₂O₃^[46] and 0.58 nm for (100) plane of cubic CsPbBr₃^[47] respectively. The interaction behaviors of α -Fe₂O₃ and CsPbBr₃ on the USGO nanosheets were firstly inspected by measuring the Raman spectra of USGO nanosheets before and after loading α -Fe₂O₃ and CsPbBr₃. As presented in Figure S5 (Supporting Information), there are two characteristic peaks at 1343 and 1583 cm⁻¹ for USGO, which can be assigned to the corresponding D-band and G-band of typical graphene oxide.^[48] Note that the peak intensity ratio between D- and G-bands for CsPbBr₃/USGO/ α -Fe₂O₃ is obviously larger than that of pristine USGO, which reveals that the incorporation of α -Fe₂O₃ and CsPbBr₃ can lead to a disordered carbon structure in USGO. The UV–vis diffuse reflectance spectra of CsPbBr₃, α -Fe₂O₃, and CsPbBr₃/USGO/ α -Fe₂O₃ in Figure S6 (Supporting Information) show that compared with CsPbBr₃ and α -Fe₂O₃, the light absorption of CsPbBr₃/USGO/ α -Fe₂O₃ composite possessed an obviously red absorption shift and enhanced absorption intensity above 475 nm, further indicating the strong interaction between CsPbBr₃, USGO, and α -Fe₂O₃.

The detailed interaction behaviors between the components in CsPbBr₃/USGO/ α -Fe₂O₃ composite were further analyzed with the aid of high-resolution X-ray photoelectron spectroscopy (XPS) measurements (Figure 3 and Figure S7, Supporting Information). As depicted in Figure 3a, the Fe 2p spectrum of pristine α -Fe₂O₃ exhibits two typical peaks at 710.8 and 724.4 eV, which can be assigned to Fe 2p_{3/2} and Fe 2p_{1/2}, respectively.^[49] There are obvious positive shifts of binding energy (\approx 0.5 eV) for both Fe 2p_{3/2} and Fe 2p_{1/2} (Figure 3a) in USGO/ α -Fe₂O₃, which could originate from the formation of C–O–Fe bonds^[36] between α -Fe₂O₃ and USGO. As a result, the C 1s peaks in USGO/ α -Fe₂O₃ show perceptible shifting to low energy in comparison with those of pristine USGO as shown in Figure 3b. Incorporating the obvious positive shift (\approx 0.3 eV) of the Fe–O–Fe bonds (at 530.0 eV) in O 1s peak (Figure S7c, Supporting Information), the presence of strong interaction between α -Fe₂O₃ and USGO is conducive to the interfacial charge transfer between them. In addition, the bonding energies of Br 3d_{5/2} (68.2 eV) and Br 3d_{3/2} (69.2 eV) in CsPbBr₃/USGO/ α -Fe₂O₃ also present obvious positive shifts (\approx 0.2 eV) with respect to those of pristine CsPbBr₃ (Figure 3c), and a decrease in the bonding energies for typical peaks of C 1s in CsPbBr₃/USGO/ α -Fe₂O₃ has been observed relative to

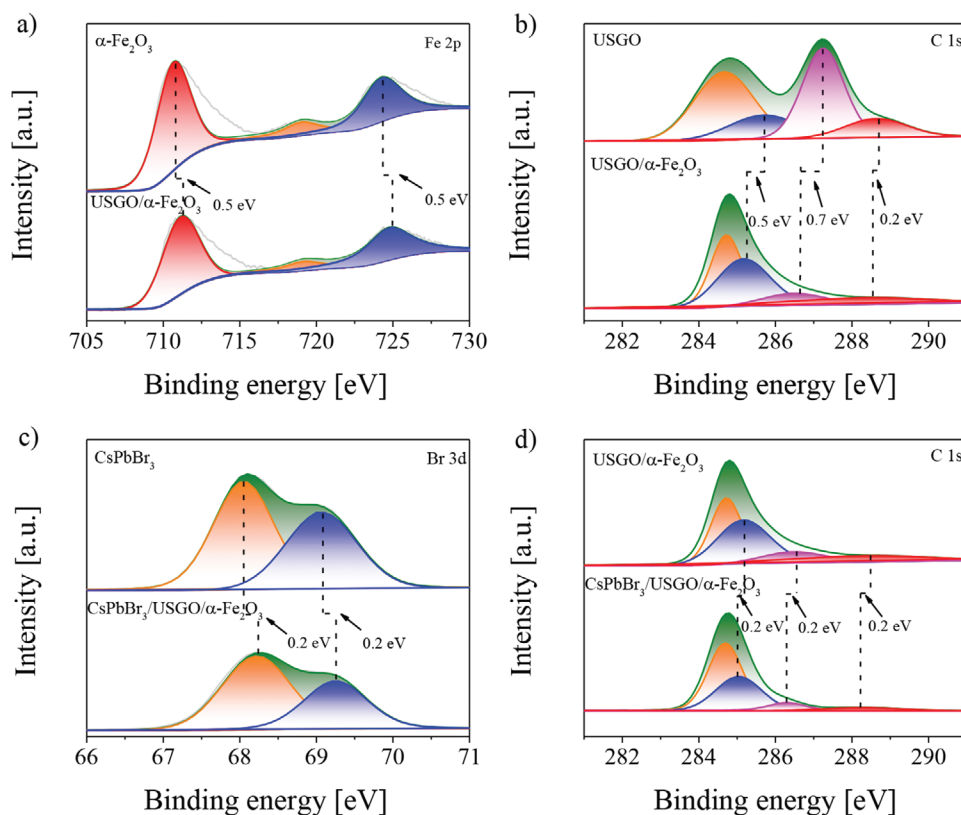


Figure 3. High-resolution XPS spectra of as-prepared samples: a) Fe 2p for $\alpha\text{-Fe}_2\text{O}_3$ and USGO/ $\alpha\text{-Fe}_2\text{O}_3$, b) C 1s for USGO and USGO/ $\alpha\text{-Fe}_2\text{O}_3$, c) Br 3d for CsPbBr₃ and CsPbBr₃/USGO/ $\alpha\text{-Fe}_2\text{O}_3$, and d) C 1s for USGO/ $\alpha\text{-Fe}_2\text{O}_3$ and CsPbBr₃/USGO/ $\alpha\text{-Fe}_2\text{O}_3$.

those in USGO/ $\alpha\text{-Fe}_2\text{O}_3$ (Figure 3d). Besides, there are negative shifts (≈ 0.2 eV) of O 1s peak (Figure S7a, Supporting Information) and positive shifts (≈ 0.3 eV) of Pb 4f peak (Figure S7b, Supporting Information) in CsPbBr₃/USGO composite with respect to those in pristine USGO and CsPbBr₃. These results indicate the existence of strong interaction between CsPbBr₃ and USGO by forming Br–O–C bonds,^[38] which can accelerate the interfacial electron transfer rate between CsPbBr₃ and USGO.

Apart from the connection pattern, it is known that the transfer processes of photogenerated carriers between two semiconductors practically associate with their energy offsets of conduction and valence band edges, which have crucial influence on the ultimate photocatalytic activity. To obtain these thermodynamic information, we first calculated the bandgaps of CsPbBr₃ and $\alpha\text{-Fe}_2\text{O}_3$ by analyzing their Tauc plots (Figure S8, Supporting Information) based on the UV–vis diffuse reflectance spectra measurements (Figure S6, Supporting Information), being 2.29 and 2.06 eV, respectively. The conduction band potentials of CsPbBr₃ and $\alpha\text{-Fe}_2\text{O}_3$ can be further derived from their Mott–Schottky plots (Figure S8, Supporting Information), being -1.07 and 0.24 V versus NHE as illustrated in Figure 4a, respectively. Thereby, the corresponding valence band potentials of CsPbBr₃ and $\alpha\text{-Fe}_2\text{O}_3$ are 1.22 and 2.30 V versus NHE (Figure 4a), which are consistent with the results of XPS valence spectra measurements (Figure S9, Supporting Information). It is worth noting that both CsPbBr₃ and $\alpha\text{-Fe}_2\text{O}_3$ are n-type semiconductors, which can be inferred

from corresponding Mott–Schottky plots with positive slopes (Figure S8, Supporting Information). Moreover, the conduction band position of $\alpha\text{-Fe}_2\text{O}_3$ is even lower than the mid-position between conduction and valence bands of CsPbBr₃, indicating that the Fermi energy level of CsPbBr₃ is higher than that of $\alpha\text{-Fe}_2\text{O}_3$. Therefore, if CsPbBr₃ and $\alpha\text{-Fe}_2\text{O}_3$ simultaneously contact the USGO electron mediator, the electrons in the surface of CsPbBr₃ tend to migrate to $\alpha\text{-Fe}_2\text{O}_3$ via USGO to realize the Fermi energy level equilibrium of the system, resulting in a built-in electric field in the interface of CsPbBr₃/USGO/ $\alpha\text{-Fe}_2\text{O}_3$ pointing from CsPbBr₃ to $\alpha\text{-Fe}_2\text{O}_3$. This orientation of built-in electric field can facilitate the photogenerated electron transfer from $\alpha\text{-Fe}_2\text{O}_3$ to CsPbBr₃, suggesting that photogenerated carrier transfer between CsPbBr₃ and $\alpha\text{-Fe}_2\text{O}_3$ complies with a Z-scheme pathway.

The time-resolved photoluminescence (TRPL) traces of samples were further recorded to check out the favorable influence of USGO on the photogenerated carrier transfer between CsPbBr₃ and $\alpha\text{-Fe}_2\text{O}_3$. As depicted in Figure 4b, the PL decay (red symbols) of CsPbBr₃ is related to the radiative and non-radiative deactivations of photogenerated excitons in CsPbBr₃. The mixture of CsPbBr₃ and $\alpha\text{-Fe}_2\text{O}_3$ (coded as CsPbBr₃: $\alpha\text{-Fe}_2\text{O}_3$) exhibits just slightly accelerated PL decay (blue symbols) in comparison with pristine CsPbBr₃, indicating the inferior charge transfer between CsPbBr₃ and $\alpha\text{-Fe}_2\text{O}_3$, which may result from the electrostatic repulsion between CsPbBr₃ and $\alpha\text{-Fe}_2\text{O}_3$ owing to their same charge nature as presented in Figure 1c. Note that loading CsPbBr₃ on the surface of

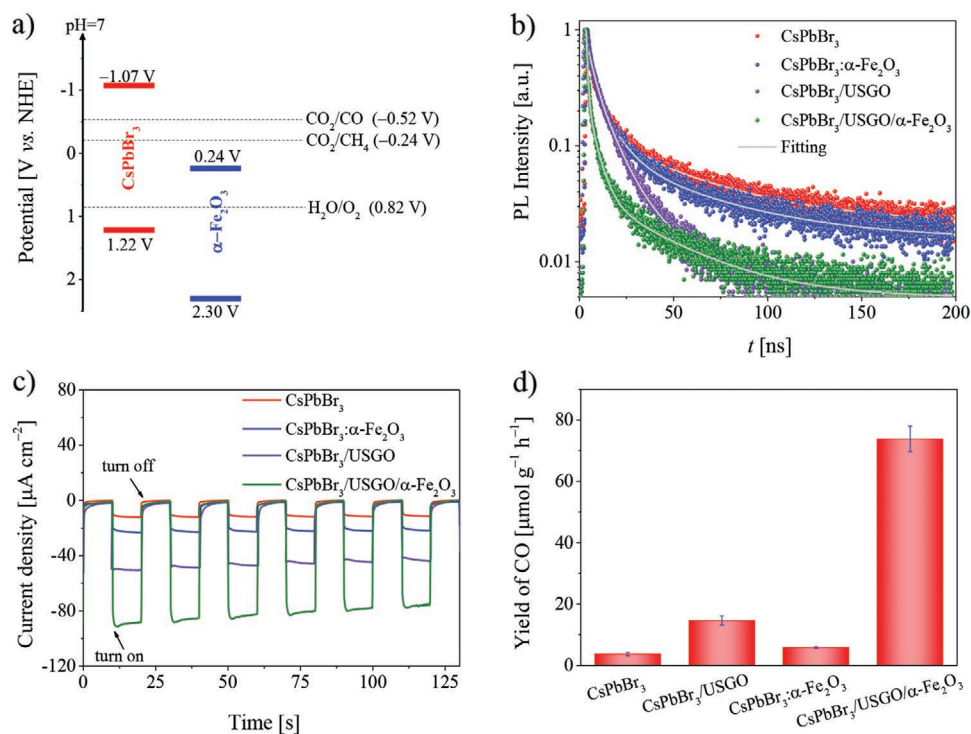


Figure 4. a) Schematic illustration of band structures for CsPbBr₃ and α -Fe₂O₃ derived from the results of flat-band potential and UV-vis absorption spectroscopy measurements. b) Time-resolved photoluminescence decay of as-prepared CsPbBr₃, CsPbBr₃: α -Fe₂O₃, CsPbBr₃/USGO, and CsPbBr₃/USGO/ α -Fe₂O₃. c) $I-t$ curves of CsPbBr₃, CsPbBr₃: α -Fe₂O₃, CsPbBr₃/USGO, and CsPbBr₃/USGO/ α -Fe₂O₃ plotted at a bias potential of -0.4 V (vs Ag/AgCl) under light illumination. d) The yield of CO generated from photocatalytic CO₂ reduction after 4 h of irradiation under 300 W Xe lamp, with the light intensity of 100 mW cm⁻².

USGO can bring forth a significantly accelerated PL decay (purple symbols) with respect to pristine CsPbBr₃, indicating the occurrence of efficient electron transfer between CsPbBr₃ and USGO due to the formation of strong chemical bonds in the interface of CsPbBr₃/USGO. Moreover, there is a further acceleration of PL decay (olive symbols) if CsPbBr₃ and α -Fe₂O₃ were simultaneously incorporated on the surface of USGO (CsPbBr₃/USGO/ α -Fe₂O₃), which can be ascribed to the excellent electron transport ability of USGO and the favorable energy offset between CsPbBr₃ and α -Fe₂O₃. All these PL evolution traces can be well fitted with a multiexponential function, and the corresponding values of amplitude-averaged lifetimes are tabulated in Table S1 (Supporting Information), being 31.3, 29.1, 20.6, and 13.9 ns for CsPbBr₃, CsPbBr₃: α -Fe₂O₃, CsPbBr₃/USGO, and CsPbBr₃/USGO/ α -Fe₂O₃, respectively.

Photocurrent response and electrochemical impedance spectroscopy (EIS) measurements were further carried out to give evidence of the benefit of USGO on the charge separation between CsPbBr₃ and α -Fe₂O₃. As presented in Figure 4c, mixing CsPbBr₃ with α -Fe₂O₃ in the absence of USGO just bring forth a slightly higher photocurrent intensity with respect to pristine CsPbBr₃, which is even lower than that of CsPbBr₃/USGO, highlighting the pivotal role of USGO in charge transfer. The photocurrent intensity of CsPbBr₃/USGO/ α -Fe₂O₃ further proves the facilitation of USGO to the interfacial charge separation, exhibiting a significant improvement of photocurrent intensity compared to pristine CsPbBr₃ as depicted in Figure 4c. Furthermore, the values of

semicircular radius in Nyquist plots for these samples are in the order: CsPbBr₃ > CsPbBr₃: α -Fe₂O₃ > CsPbBr₃/USGO > CsPbBr₃/USGO/ α -Fe₂O₃ (Figure S10, Supporting Information), indicating that the charge-transfer resistance obviously decreased for CsPbBr₃/USGO/ α -Fe₂O₃, as evidenced by the corresponding fitting results (22 614 Ω for CsPbBr₃, 12 627 Ω for CsPbBr₃: α -Fe₂O₃, 8679 Ω for CsPbBr₃/USGO, and 4573 Ω for CsPbBr₃/USGO/ α -Fe₂O₃). These results are consistent with the photocurrent response measurements, once again demonstrating the favorable influence of USGO on the interfacial charge transfer.

The photocatalytic performances of CsPbBr₃, α -Fe₂O₃, CsPbBr₃/USGO, and CsPbBr₃/USGO/ α -Fe₂O₃ for CO₂ reduction were evaluated in CO₂-saturated acetonitrile/water solution under simulated sunlight irradiation with Xe lamp coupled with a 400 nm filter, and the light intensity was adjusted to 100 mW cm⁻² by calibrating with a NREL-calibrated Si solar cell. Herein, there is only very small amount of water in the reaction system, because of the instability of halide perovskite in the reaction system with a large amount of water. For these CsPbBr₃-based photocatalysts, the results of chromatographic analyses show that the main reduction product is CO, and only negligible CH₄ and H₂ can be detected. Although the CO₂-to-CH₄ conversion by the photogenerated electrons in these catalysts is thermodynamically permissible, the unfavorable evolution of CH₄ may originate from the rapid desorption of the reaction intermediate, that is CO,^[50] from the surface of the catalyst. This phenomenon is consistent with

the common observation in the photocatalytic systems with CsPbBr₃ as photocatalyst.^[16–19] As depicted in Figure 4d, the yield of CO is only 3.7 μmol g⁻¹ h⁻¹ with pristine CsPbBr₃ as photocatalyst, owing to the insufficient charge separation. It is noted that no reduction product can be detected with pure α-Fe₂O₃ as photocatalyst, because the conduction band potential (0.24 V vs NHE) of α-Fe₂O₃ is not high enough to trigger CO₂ reduction reaction. Under the same condition, loading CsPbBr₃ on USGO can bring forth an obvious improvement of photocatalytic activity as presented in Figure 4d. An obviously enhanced yield of 14.6 μmol g⁻¹ h⁻¹ can be achieved for CO₂-to-CO conversion, owing to the strong interaction between CsPbBr₃ and USGO.

More importantly, if CsPbBr₃ and α-Fe₂O₃ were simultaneously incorporated onto the USGO nanosheet, the activity of photocatalytic CO₂ reduction can be further significantly enhanced as shown in Figure 4d. CsPbBr₃/USGO/α-Fe₂O₃ composite achieves an exciting yield of 73.8 μmol g⁻¹ h⁻¹ for CO₂-to-CO conversion, which is over 19 times higher than that of pure CsPbBr₃. To the best of our knowledge, the electron consumption rate ($R_{\text{electron}} = 147.6 \mu\text{mol g}^{-1} \text{h}^{-1}$) with CsPbBr₃/USGO/α-Fe₂O₃ as photocatalyst is well above that of reported metal-halide perovskite materials photocatalysts with desirable water as electron source and under 1 sun light irradiation (Table S2, Supporting Information). In addition, to evaluate the superiority of USGO for accelerating the charge transfer between CsPbBr₃ and α-Fe₂O₃, the photocatalytic activity of CsPbBr₃:α-Fe₂O₃ composite has also been assessed under the same condition. As shown in Figure 4d, CsPbBr₃:α-Fe₂O₃ composite just exhibits a slightly improved photocatalytic activity (5.8 μmol g⁻¹ h⁻¹) compared to pristine CsPbBr₃, highlighting the important role of USGO in accelerating the interfacial charge transfer rate by providing an electron transport freeway. Besides, the time-dependent data for the evolution of CO (Figure S11, Supporting Information) and the XRD patterns of CsPbBr₃/USGO/α-Fe₂O₃ after photoreduction of CO₂ (Figure S12, Supporting Information) suggest that the catalytic activity and crystal structures of CsPbBr₃ and α-Fe₂O₃ were basically maintained in CsPbBr₃/USGO/α-Fe₂O₃ after photocatalytic reaction for 8 h. The slightly increased diffraction peaks of CsPbBr₃/USGO/α-Fe₂O₃ may result from the occurrence of a certain degree of aggregation after reaction. Furthermore, the reusability of CsPbBr₃/USGO/α-Fe₂O₃ composite was also tested with two consecutive cycles of the photocatalytic experiments. As shown in Figure S13 (Supporting Information), after two cycles, the activity of CsPbBr₃/USGO/α-Fe₂O₃ was remained for 90%, indicating the relatively stability of CsPbBr₃/USGO/α-Fe₂O₃ composite in the reaction system containing small amount of water.

The origin of reduction product CO was further identified by performing a series of reference experiments with CsPbBr₃/USGO/α-Fe₂O₃ as photocatalyst. There is negligible light response in the absence of light irradiation or photocatalyst in the reaction system, suggesting that CO₂-to-CO conversion is triggered by the photogenerated carriers in CsPbBr₃/USGO/α-Fe₂O₃. In addition, replacing CO₂ with N₂ also results in negligible light response, indicating that CO is produced from CO₂ reduction. This speculation has been further confirmed by isotope tracking experiment with ¹³CO₂ instead of CO₂, where the major reaction product ¹³CO with *m/z* value of 29 and negligible

¹³CH₄ with *m/z* value of 17 (Figure S14, Supporting Information) can be clearly observed by the gas chromatography/mass spectrometry analysis. Moreover, oxidation product O₂ can also be detected in the gas products, and the ratio of the amounts of CO and O₂ is close to 2:1 (Figure S15, Supporting Information), indicating that the photogenerated holes in CsPbBr₃/USGO/α-Fe₂O₃ are mainly consumed by the water oxidation reaction. Further H₂¹⁸O isotope labeling experiment demonstrated that O₂ is the product of water oxidation, where the oxidation production ¹⁸O₂ (*m/z* = 36) can be clearly observed in the result of gas chromatography/mass spectrometry analysis (Figure S16, Supporting Information).

From the thermodynamic point of view, the result of significantly enhanced performance of CsPbBr₃/USGO/α-Fe₂O₃ indicates that the photogenerated carrier separation in CsPbBr₃/USGO/α-Fe₂O₃ is Z-scheme mechanism. If the pathway of interfacial charge transfer between CsPbBr₃ and α-Fe₂O₃ complies with traditional type-II heterojunction, the photogenerated electrons in CsPbBr₃ should transfer to α-Fe₂O₃ via USGO mediator. As shown in Figure 4a, the conduction band potential of α-Fe₂O₃ is lower than the reduction potential of CO₂-to-CO conversion (-0.52 V vs NHE). The photogenerated electrons in α-Fe₂O₃ have no driving force to trigger the reduction reaction of CO₂, which contrasts with the results of photocatalytic measurements. To further confirm the Z-scheme mechanism in CsPbBr₃/USGO/α-Fe₂O₃ system, we resorted to in situ irradiated XPS (ISI-XPS) measurement^[51,52] to inspect the orientation of interfacial charge transfer between CsPbBr₃ and α-Fe₂O₃. As presented in Figure 5a, without light irradiation, the Br 3d spectrum of CsPbBr₃/USGO/α-Fe₂O₃ could be resolved into two typical peaks corresponding to Br 3d_{5/2} (68.2 eV) and Br 3d_{3/2} (69.2 eV). In addition, Pb 4f spectrum of CsPbBr₃/USGO/α-Fe₂O₃ exhibits two characteristic peaks at 138.3 and 143.2 eV (Figure 5b), which can be assigned to Pb 4f_{7/2} and Pb 4f_{5/2}, respectively. Light irradiation brings forth an obvious negative shift (≈0.3 eV) of binding energies for both Br 3d and Pb 4f, indicating an increased electron density around the Br and Pb nucleus by accumulating electrons. On the other hand, a characteristic peak at 711.3 eV for Fe 2p_{3/2} can be clearly observed in Fe 2p spectrum of CsPbBr₃/USGO/α-Fe₂O₃ without light irradiation (Figure 5c). Meanwhile, the characteristic peak position of Fe 2p_{1/2} at 725.3 eV can also be obtained by fitting the Fe 2p spectrum with considering the interference of Cs 3d signal (Figure 5d). Upon light irradiation, both Fe 2p_{1/2} and Fe 2p_{3/2} exhibit positive shifted binding energies, being 711.6 and 725.5 eV, respectively, which suggests the occurrence of holes accumulation in α-Fe₂O₃. These phenomena of binding energy shifting induced by light irradiation confirm that photogenerated electrons in α-Fe₂O₃ transfer to CsPbBr₃ through USGO electron mediator, which is in line with Z-scheme mechanism.

3. Conclusion

In summary, we have successfully constructed an efficient halide-perovskite based all-solid-state Z-scheme system using USGO as electron mediator, which presents an exciting electron consumption rate of 147.6 μmol g⁻¹ h⁻¹ for the conversion of

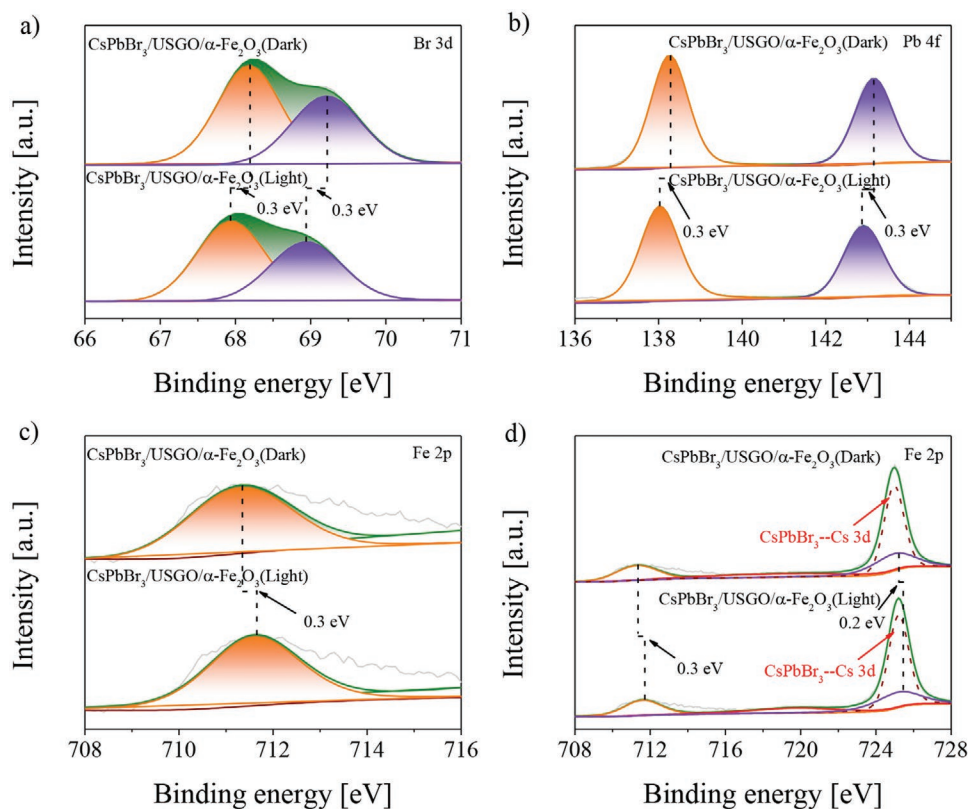


Figure 5. High-resolution XPS spectra of CsPbBr₃/USGO/ α -Fe₂O₃ in the dark or under 300 W Xe lamp irradiation with a 400 nm filter: a) Br 3d, b) Pb 4f, c) Fe 2p_{3/2}, and d) the full-spectrum of Fe 2p.

photocatalytic CO₂-to-CO with water as the sacrificial reductant. XPS measurements revealed that α -Fe₂O₃ and CsPbBr₃ display strong interaction with USGO by forming chemical bonds. With respect to the mixture of α -Fe₂O₃ and CsPbBr₃, the introduction of USGO can bring forth a significant improvement of charge separation efficiency between α -Fe₂O₃ and CsPbBr₃ as demonstrated by the photophysical and electrochemical measurements. Further ISI-XPS characterization confirmed the pathway of interfacial charge transfer between CsPbBr₃ and α -Fe₂O₃, and gave an obvious evidence of the formation of Z-scheme heterojunction between CsPbBr₃ and α -Fe₂O₃. This work provides an important inspiration for the utilization of halide perovskite as well as various low-cost semiconductors in the field of artificial photosynthesis.

Supporting Information

Supporting Information is available from the Wiley Online Library or from the author.

Acknowledgements

Y.-F.M. and W.Z. contributed equally to this work. This work was financially supported by Natural Science Foundation of Tianjin City (17JCJQJC43800), National Key R&D Program of China (2017YFA0700104), NSFC (21790052 and 21702146), and the 111 Project (D17003).

Conflict of Interest

The authors declare no conflict of interest.

Keywords

charge transfer, CO₂ reduction, perovskite nanocrystals, photocatalysis, Z-scheme systems

Received: April 2, 2020

Revised: April 29, 2020

Published online:

- [1] X. Li, J. Yu, M. Jaroniec, X. Chen, *Chem. Rev.* **2019**, *119*, 3962.
- [2] H.-L. Wu, X.-B. Li, C.-H. Tung, L.-Z. Wu, *Adv. Mater.* **2019**, *31*, 1900709.
- [3] J. Ran, M. Jaroniec, S.-Z. Qiao, *Adv. Mater.* **2018**, *30*, 1704649.
- [4] J. H. Montoya, L. C. Seitz, P. Chakhranont, A. Vojvodic, T. F. Jaramillo, J. K. Nørskov, *Nat. Mater.* **2017**, *16*, 70.
- [5] X. Liu, S. Inagaki, J. Gong, *Angew. Chem., Int. Ed.* **2016**, *55*, 14924.
- [6] K. K. Sakimoto, A. B. Wong, P. Yang, *Science* **2016**, *351*, 74.
- [7] J. L. White, M. F. Baruch, J. E. Pander III, Y. Hu, I. C. Fortmeyer, J. E. Park, T. Zhang, K. Liao, J. Gu, Y. Yan, T. W. Shaw, E. Abelev, A. B. Bocarsly, *Chem. Rev.* **2015**, *115*, 12888.
- [8] S. Berardi, S. Drouet, L. Francàs, C. Gimbert-Suriñach, M. Guttentag, C. Richmond, T. Stoll, A. Llobet, *Chem. Soc. Rev.* **2014**, *43*, 7501.

- [9] S. N. Habisreutinger, L. Schmidt-Mende, J. K. Stolarczyk, *Angew. Chem., Int. Ed.* **2013**, *52*, 7372.
- [10] S. C. Roy, O. K. Varghese, M. Paulose, C. A. Grimes, *ACS Nano* **2010**, *4*, 1259.
- [11] Q. A. Akkerman, G. Rainò, M. V. Kovalenko, L. Manna, *Nat. Mater.* **2018**, *17*, 394.
- [12] M. V. Kovalenko, L. Protesescu, M. I. Bodnarchuk, *Science* **2017**, *358*, 745.
- [13] X. Li, F. Cao, D. Yu, J. Chen, Z. Sun, Y. Shen, Y. Zhu, L. Wang, Y. Wei, Y. Wu, H. Zeng, *Small* **2017**, *13*, 1603996.
- [14] L.-Y. Wu, Y.-F. Mu, X.-X. Guo, W. Zhang, Z.-M. Zhang, M. Zhang, T.-B. Lu, *Angew. Chem., Int. Ed.* **2019**, *58*, 9491.
- [15] Z.-C. Kong, J.-F. Liao, Y.-J. Dong, Y.-F. Xu, H.-Y. Chen, D.-B. Kuang, C.-Y. Su, *ACS Energy Lett.* **2018**, *3*, 2656.
- [16] J. Hou, S. Cao, Y. Wu, Z. Gao, F. Liang, Y. Sun, Z. Lin, L. Sun, *Chem. - Eur. J.* **2017**, *23*, 9481.
- [17] Y.-F. Xu, M.-Z. Yang, B.-X. Chen, X.-D. Wang, H.-Y. Chen, D.-B. Kuang, C.-Y. Su, *J. Am. Chem. Soc.* **2017**, *139*, 5660.
- [18] M. Ou, W. Tu, S. Yin, W. Xing, S. Wu, H. Wang, S. Wan, Q. Zhong, R. Xu, *Angew. Chem., Int. Ed.* **2018**, *57*, 13570.
- [19] Y.-F. Mu, W. Zhang, X.-X. Guo, G.-X. Dong, M. Zhang, T.-B. Lu, *ChemSusChem* **2019**, *12*, 4769.
- [20] A. J. Bard, *J. Photochem.* **1979**, *10*, 59.
- [21] H. Tada, T. Mitsui, T. Kiyonaga, T. Akita, K. Tanaka, *Nat. Mater.* **2006**, *5*, 782.
- [22] J. Yu, S. Wang, J. Low, W. Xiao, *Phys. Chem. Chem. Phys.* **2013**, *15*, 16883.
- [23] Y. Jiang, J.-F. Liao, H.-Y. Chen, H.-H. Zhang, J.-Y. Li, X.-D. Wang, D.-B. Kuang, *Chem* **2020**, *6*, 766.
- [24] Y. Wang, H. Suzuki, J. Xie, O. Tomita, D. J. Martin, M. Higashi, D. Kong, R. Abe, J. Tang, *Chem. Rev.* **2018**, *118*, 5201.
- [25] Q. Wang, T. Hisatomi, Y. Suzuki, Z. Pan, J. Seo, M. Katayama, T. Minegishi, H. Nishiyama, T. Takata, K. Seki, A. Kudo, T. Yamada, K. Domen, *J. Am. Chem. Soc.* **2017**, *139*, 1675.
- [26] A. Iwase, S. Yoshino, T. Takayama, Y. H. Ng, R. Amal, A. Kudo, *J. Am. Chem. Soc.* **2016**, *138*, 10260.
- [27] H. Li, W. Tu, Y. Zhou, Z. Zou, *Adv. Sci.* **2016**, *3*, 1500389.
- [28] P. Zhou, J. Yu, M. Jaroniec, *Adv. Mater.* **2014**, *26*, 4920.
- [29] K. Maeda, *ACS Catal.* **2013**, *3*, 1486.
- [30] S. Shen, S. A. Lindley, X. Chen, J. Z. Zhang, *Energy Environ. Sci.* **2016**, *9*, 2744.
- [31] M. Mishra, D.-M. Chun, *Appl. Catal., A* **2015**, *498*, 126.
- [32] A. J. Cowan, C. J. Barnett, S. R. Pendlebury, M. Barroso, K. Sivula, M. Grätzel, J. R. Durrant, D. R. Klug, *J. Am. Chem. Soc.* **2011**, *133*, 10134.
- [33] K. Sivula, F. L. Formal, M. Grätzel, *ChemSusChem* **2011**, *4*, 432.
- [34] Y. Lin, G. Yuan, S. Sheehan, S. Zhou, D. Wang, *Energy Environ. Sci.* **2011**, *4*, 4862.
- [35] M.-Q. Yang, N. Zhang, M. Pagliaro, Y.-J. Xu, *Chem. Soc. Rev.* **2014**, *43*, 8240.
- [36] Z. Pan, G. Zhang, X. Wang, *Angew. Chem., Int. Ed.* **2019**, *58*, 7102.
- [37] D. R. Dreyer, S. Park, C. W. Bielawski, R. S. Ruoff, *Chem. Soc. Rev.* **2010**, *39*, 228.
- [38] X.-X. Guo, S.-F. Tang, Y.-F. Mu, L.-Y. Wu, G.-X. Dong, M. Zhang, *RSC Adv.* **2019**, *9*, 34342.
- [39] X. Li, Y. Wang, H. Sun, H. Zeng, *Adv. Mater.* **2017**, *29*, 1701185.
- [40] J. De Roo, M. Ibáñez, P. Geiregat, G. Nedelcu, W. Walravens, J. Maes, J. C. Martins, I. Van Driessche, M. V. Kovalenko, Z. Hens, *ACS Nano* **2016**, *10*, 2071.
- [41] L. Zhang, J. Liang, Y. Huang, Y. Ma, Y. Wang, Y. Chen, *Carbon* **2009**, *47*, 3365.
- [42] L. Zhang, X. Li, Y. Huang, Y. Ma, X. Wan, Y. Chen, *Carbon* **2010**, *48*, 2361.
- [43] S. Stankovich, D. A. Dikin, G. H. B. Dommett, K. M. Kohlhaas, E. J. Zimney, E. A. Stach, R. D. Piner, S. T. Nguyen, R. S. Ruoff, *Nature* **2006**, *442*, 282.
- [44] H. Zhang, A. Xie, C. Wang, H. Wang, Y. Shen, X. Tian, *J. Mater. Chem. A* **2013**, *1*, 8547.
- [45] T. Zhang, C. Zhu, Y. Shi, Y. Li, S. Zhu, D. Zhang, *Mater. Lett.* **2017**, *205*, 10.
- [46] D. Li, R. Xu, Y. Jia, P. Ning, K. Li, *Chem. Phys. Lett.* **2019**, *731*, 136623.
- [47] J. Liu, B. Shabbir, C. Wang, T. Wan, Q. Ou, P. Yu, A. Tadich, X. Jiao, D. Chu, D. Qi, D. Li, R. Kan, Y. Huang, Y. Dong, J. Jasieniak, Y. Zhang, Q. Bao, *Adv. Mater.* **2019**, *31*, 1901644.
- [48] Y. Zhu, S. Murali, W. Cai, X. Li, J. W. Suk, J. R. Potts, R. S. Ruoff, *Adv. Mater.* **2010**, *22*, 3906.
- [49] X. Hu, J. C. Yu, J. Gong, Q. Li, G. Li, *Adv. Mater.* **2007**, *19*, 2324.
- [50] H. Rao, L. C. Schmidt, J. Bonin, M. Robert, *Nature* **2017**, *548*, 74.
- [51] X. G. Liu, G. J. Dong, S. P. Li, G. X. Lu, Y. P. Bi, *J. Am. Chem. Soc.* **2016**, *138*, 2917.
- [52] J. Low, B. Dai, T. Tong, C. Jiang, J. Yu, *Adv. Mater.* **2019**, *31*, 1802981.